Buoyancy characteristic analysis and optimization of precast concrete slab track during casting process of self-compacting concrete

Received 6 January 2025
Revised 14 January 2025
Accepted 24 January 2025

Pengsong Wang
Railway Science and Technology Research and Development Center, China Academy of Railway Sciences Corporation Limited, Beijing, China
Tao Xin
School of Civil Engineering, Beijing Jiaotong University, Beijing, China
Peng Chen
Beijing Urban Construction Design and Development Group Corporation Limited, Beijing, China
Sen Wang
School of Civil Engineering, Beijing Jiaotong University, Beijing, China, and
Di Cheng
Railway Science and Technology Research and Development Center, China Academy of Railway Sciences Corporation Limited, Beijing, China

Abstract

Purpose – The precast concrete slab track (PST) has advantages of fewer maintenance frequencies, better smooth rides and structural stability, which has been widely applied in urban rail transit. Precise positioning of precast concrete slab (PCS) is vital for keeping the initial track regularity. However, the cast-in-place process of the self-compacting concrete (SCC) filling layer generally causes a large deformation of PCS due to the water-hammer effect of flowing SCC, even cracking of PCS. Currently, the buoyancy characteristic and influencing factors of PCS during the SCC casting process have not been thoroughly studied in urban rail transit.

Design/methodology/approach – In this work, a Computational Fluid Dynamics (CFD) model is established to calculate the buoyancy of PCS caused by the flowing SCC. The main influencing factors, including the inlet speed and flowability of SCC, have been analyzed and discussed. A new structural optimization scheme has been proposed for PST to reduce the buoyancy caused by the flowing SCC.

Findings – The simulation and field test results showed that the buoyancy and deformation of PCS decreased obviously after adopting the new scheme.

Originality/value – The findings of this study can provide guidance for the control of the deformation of PCS during the SCC construction process.

Keywords Casting process, Buoyancy characteristics, Precast concrete slab track, Simulation, Field test, Optimization

Paper type Research paper

This research work was funded by the Science Technology Research and Development Program of China Academy of Railway Sciences Co., Ltd (No: 2023YJ251).

Conflict of interest: The authors declare that they have no known competing financial interests or personal relationships that could have appeared to influence the work reported in this paper.

Railway Sciences
Vol. 4 No. 2, 2025
pp. 159-173
Emerald Publishing Limited
e-ISSN: 2755-0915
p-ISSN: 2755-0907
DOI 10.1108/RS-01-2025-0002

1. Introduction

Urban rail transit (mainly subway) has rapidly developed in recent years (Jiang, Ma, Li, Liu, & Li, 2019; Liang *et al.*, 2019, 2022), which plays an important role in solving the problems of urban development and citizen travel. For urban rail transit lines, the track structure is vital for guiding train operations and bearing the trains loads. In the past, the cast-in-place track beds were mainly adopted in urban rail transit, which had problems such as poor smoothness of the line, serious vibration and noise disturbance to residents, complex construction procedures, low operational efficiency and frequent maintenance and repair. Thus, the precast concrete slab track (PST) is introduced to urban rail transit from high-speed railway to increase the inherent resilient quality of the tracks, provide smooth rides and reduce the maintenance frequencies. Research has shown that PSTs can reduce maintenance costs by 70–90% and decrease the weight and height of track structures. The PSTs have been widely applied in high-speed railways in the past few decades (Chen, Wang *et al.*, 2024; Chen, Zhang, *et al.*, 2024; Liang *et al.*, 2019). Some of them include the Shinkansen system (Ando, Sunaga, Aoki, & Haga, 2001) developed in Japan, the Bögl system developed in Germany, the Slab Track Austria system developed in Austria and the China Railway Track System (CRTS) series systems developed in China.

The typical PST system in urban rail transit is generally composed of three layers. The precast concrete slab (PCS) lies at the top, the grouting layer exists at the middle and the base course is at the bottom, as shown in Figure 1. In the grouting process, the PCS is fixed above the base course, and the grouting layer was grouted through the reserved holes on PCS using the cement-based materials.

The grouting layer serves as a critical component within the structure system of PST, with the *in situ* casting process directly impacting the quality of the track structure. The PST imposes rigorous requirements on the positional accuracy of the track slab to ensure optimal rail smoothness. Consequently, the maximum allowable deviation of the track slab's position after the casting of self-compacting concrete (SCC) is 2 mm, while the maximum acceptable deviation of the thickness of SCC is 10 mm. However, practical engineering often witnesses deviations exceeding the limits. This phenomenon arises from an uplift force exerted on the lower surface of the PCS (Su, Chong, Xie, Xie, & Zeng, 2024; Zhang *et al.*, 2024), inherent to the cast-in-place procedure for the SCC filling layer. To reduce the vertical upward deformation caused by the SCC, temporary constraints are placed on the track slab during the casting stage, utilizing steel limiting beams, as shown in Plate 1.

Despite the implementation of limiting beams, the deformation still surpasses the allowable limits in practical engineering. For instance, Shu *et al.* indicated that the upward deformation reaches 2.7 mm if the duration of the SCC's casting is approximately 2.5 min. The track slab with excessive upward deformation increases the workload of the fine-tuning phase (Xu, Liu, Yang, & Yang, 2013), and it usually needs specific under-rail pads to adjust the position of rails. This causes the replacement of normal under-rail pads and increases the cost and waste of

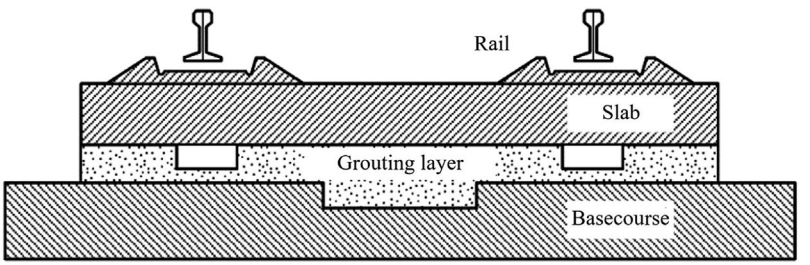

Source(s): Authors' own work

Figure 1. The structural composition of typical PST

Source(s): Authors' own work

Plate 1. The steel limiting beams

resources. However, the majority of research has primarily focused on the interfacial damage (Jiang, Xie, Wu, & Long, 2020, 2021; Wang *et al.*, 2022) or concrete cracks (Guo, Huang, Zhao, & Wei, 2021; Zhang *et al.*, 2022) of the PST. There are only a few studies that have investigated the impact of material and construction factors on the deformation of PCS. The current understanding of the up-floating characteristic of the PCS mainly comes from the empirical summary. Ou and Chen (2017) obtained the up-floating displacements of PCS in the grouting process of the CRTSII slab track, and some measures were proposed to reduce the buoyancy. Ren (2021) proposed that the total time of the grouting process should be more than 3 min to weaken the water-hammer effect of the fresh cement-based material. Tan, Xie, Yang, and Li (2017) analyzed the up-floating displacement results of PCS under different grouting methods in grouting process of the CRTSIII slab track. Cao proposed that the inlet speed of cement-based materials should be reduced in the later phase of the grouting process to weaken the water-hammer effect of the fresh cement-based material (Cao, 2020). There is a lack of theoretical understanding and analysis on the up-floating characteristics of PCS in the grouting process. The evolution characteristics of buoyancy on PCS and the main factors to control the up-floating of PCS are not clear. Xu *et al.* (2013) analyzed the track slab's deformation during the casting process of SCC, revealing that the up-lift force acting on the track slab is proportionate to the flowing speed of SCC. Nevertheless, all of these literatures are short technical notes and written in Chinese. The mechanisms of the upward deformation of the track slab have not been fully studied.

Hence, the cast-in-place process of SCC was simulated by the CFD method in this manuscript. The evolution characteristics of buoyancy on PCS were analyzed. The parameter influence analysis was carried out to determine the main factors affecting the buoyancy. A structural optimization scheme was proposed to reduce the buoyancy. The buoyancy and upward deformation characteristics of PST after optimization were demonstrated by simulation and test.

2. Rheological properties of fresh SCC

The rheological properties of fresh SCC should be determined before simulating the grouting process of PST. The rheological constitutive model is selected to describe the flow characteristics of SCC in this section, and the slump test is carried out to evaluate the flowability of SCC. The concrete slump process is simulated using the CFD method, and the rheological parameters of fresh SCC are determined through comparison of the simulation and test results.

2.1 Rheological constitutive model of fresh SCC

Fresh SCC belongs to a non-Newtonian fluid (Abedi, Lin, & Ji, 2023), which only undergoes irreversible deformation and flow behaviors when subjected to the shear stress greater than the yield shear stress. Due to different preparation technology and mix proportions (Li, Huang, Xie, Yi, & Wang, 2017), the fresh SCC also has the properties of shear-thickening and shear-thinning.

The Bingham model and Herschel Bulkley (H-B) model are commonly used to describe the rheological characteristics of SCC. The H-B model is adopted in the simulation, considering its higher accuracy compared with the experimental results (Li & Xu, 2013), as shown in Equation (1).

$$\mu\left(\dot{\gamma}\right) = \begin{cases} \mu_0 & \dot{\gamma} < \dfrac{\tau_0}{\mu_0} \\ \dfrac{\tau_0 + k\left(\dot{\gamma} - \frac{\tau_0}{\mu_0}\right)^n}{\dot{\gamma}} & \dot{\gamma} \geq \dfrac{\tau_0}{\mu_0} \end{cases} \tag{1}$$

where τ_0 represents the yield shear stress, μ_0 represents the zero-shear viscosity, k represents the consistency index and n represents the flow behavior index.

2.2 The fresh SCC slump test

The slump test is generally carried out to evaluate the flowability of fresh concrete. The slump test instrument mainly contains a bucket and measuring platform, as shown in Plate 2(a). The top radius of the standard slump bucket R_t is 50 mm, the bottom radius R_b is 100 mm and the height of bucket H_0 is 300 mm. The slump test results are shown in Plate 2(b). The slump s, the spread S_f and the time T_{500}, which represents the spread reaching 500 mm are 273 mm, 668 mm and 3.9 s, respectively.

2.3 Simulation of SCC slump process

To determine the rheological parameters of fresh SCC, the fresh SCC slump process was simulated by the CFD method. The CFD model is discretized by a polyhedral mesh, and the mesh size is around 5 mm, as shown in Figure 2(a). The initial volume fraction distribution of SCC is shown in Figure 2(b).

Slump bucket and measuring platform

(a)

Test results

(b)

Source(s): Authors' own work

Plate 2. The fresh SCC slump test

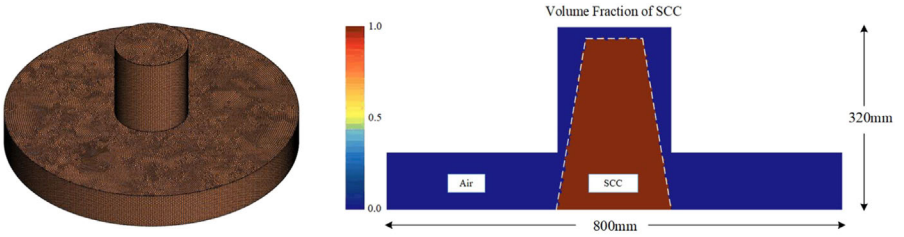

The mesh of model
(a)

The initial volume distribution of SCC
(b)

Source(s): Authors' own work

Figure 2. The CFD model of simulating SCC slump process

In the space of the slump bucket, the volume fraction of SCC is 1 and the other space is 0. The volume of fluid method is adopted to capture the interface between SCC and air (Xie, Wei, Liu, & Liu, 2023). The bottom surface is set as a wall, and no relative sliding between SCC and the bottom surface is assumed. The side and top surfaces are set as pressure-outlet of air, and the relative pressure is 0 Pa. The model is solved using implicit methods. The time step is 0.002 s. The total physical time is set as 30 s, considering that the shape of SCC is roughly fixed around 30 s in the slump process (Mu, Li, Hao, Liu, & Shen, 2023). According to the empirical formula proposed by Roussel (2007), the correlation between yield shear stress τ_0 and the spread S_f can be written in Equation (2), and it can be inferred that the yield shear stress τ_0 is 29.5 Pa.

$$\tau_0 = \frac{225\rho g V^2}{4\pi^2 S_f{}^5} \tag{2}$$

where τ_0 represents the yield shear stress, ρ represents the density, S_f represents the spread, g represents the gravitational acceleration and V represents the volume of SCC.

The consistency index k and the flow behavior index n are evaluated with reference to the simulation results of the SCC slump process in Li, Mu, Wang, Liu, and Du (2021). It is found that the simulation and test results have a good agreement when k is 70Pa·s$^{1.38}$ and n is 1.38. Adopting the parameters, the simulation results at $t = 3.8$ s and $t = 30.0$ s are shown in Figures 3 and 4, respectively. The slump s, the spread S_f and the time T_{500} are 271 mm, 674 mm and

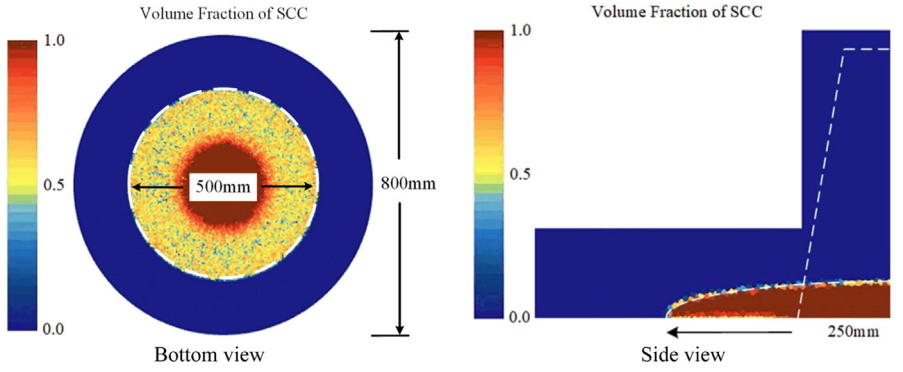

Bottom view
(a)

Side view
(b)

Source(s): Authors' own work

Figure 3. The simulation results of slump test at $t = 3.8$s

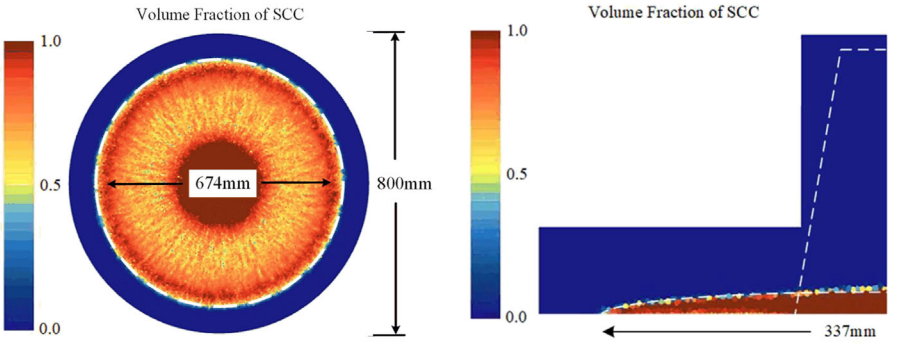

Source(s): Authors' own work

Figure 4. The simulation results of slump test at t = 30.0s

3.8 s, with errors of 0.7, 0.3 and 2.6% compared with field test results. It indicates that the H-B model and the above parameters can accurately describe the flowability of SCC.

3. Numerical simulation of the grouting process

The grouting process of PST was simulated by CFD method based on the rheological properties of SCC. The evolution characteristic of buoyancy on PCS was analyzed. The size of PCS is 3,450 mm × 2,200 mm × 200 mm. The density of PCS is 2,400 kg, and the total mass of PCS is 3,290 kg. Thus, the gravity load for half of PCS is 16.12 kN with g is selected as 9.8 m/s^2.

3.1 Numerical model

In the grouting process, the PCS is fixed above the base course, and the molds are installed around it, as shown in Figure 5. To avoid the excessive up-floating displacement, the PCS is held down using the steel beams. The air is mainly discharged from the grouting holes reserved on the PCS. According to the grouting methods of PST, the CFD model to simulate the

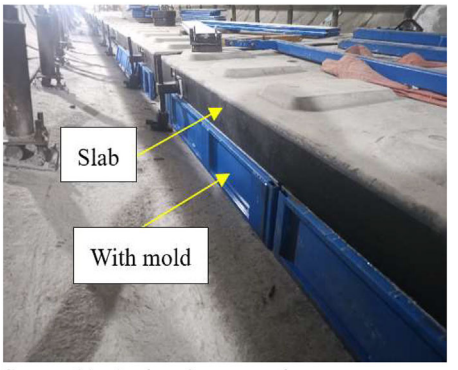

Source(s): Authors' own work

Figure 5. The installation of PCS in the grouting process

grouting process is established in Figure 6. In the simulation, the PCS is fixed. The fluid computing domain is in the space of the grouting layer. The total pressure on top surfaces is regarded as the buoyancy on PCS in grouting process. Considering the symmetry of the track structure, half of it is simulated to improve computing efficiency.

One grouting hole on PCS is set as the velocity-inlet of SCC, and the other one is set as the pressure-outlet of air, which is also called the observation hole. The surface along the longitudinal centerline is set as symmetry. Other surfaces are set as wall. The initial inlet speed of SCC is assumed to be 0.1 m/s. The grouting process will stop once the liquid level of SCC is even with the top rim of the observation hole, and the inlet speed of SCC is set as 0 m/s at the same time.

3.2 Evolution characteristic of buoyancy

The evolution characteristic of buoyancy on PCS obtained from the simulation is shown in Figure 7. The change of buoyancy can be divided into three phases.

In the 1st phase, the PCS is not subjected to buoyancy. The grouting statue is shown in Figure 8. The space of the t grouting layer is filled with little SCC. The SCC and the bottom surface of PCS are not in contact. The SCC mainly accumulates near the grouting hole.

In the 2nd phase, the SCC and the bottom surface of PCS are in contact. The grouting statue is shown in Figure 9. The buoyancy on PCS gradually increases from 0 kN to the maximum 21.08 kN. The rapid increase in buoyancy is mainly concentrated in the later stage, which is caused by the rapid rise of the liquid level of SCC in the observation hole. The maximum

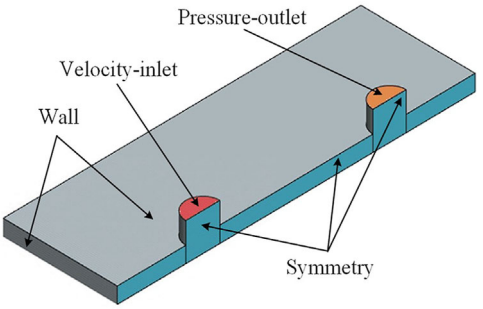

Source(s): Authors' own work

Figure 6. The CFD model to simulate the grouting process

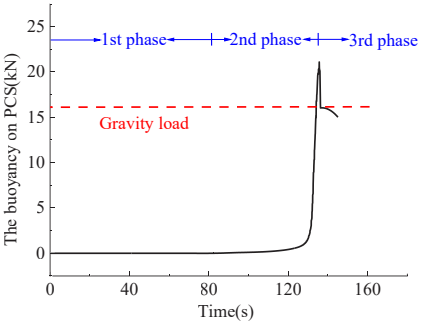

Source(s): Authors' own work

Figure 7. The time-history curve of buoyancy on PCS

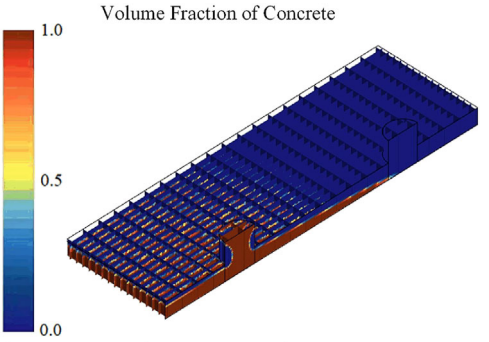

Source(s): Authors' own work

Figure 8. The grouting statue at 1st phase

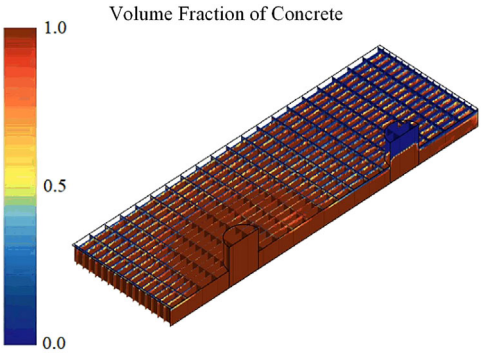

Source(s): Authors' own work

Figure 9. The grouting statue at 2nd phase

buoyancy occurs at the time when the liquid level of SCC is even with the top rim of the observation hole, which is 130.8% of its gravity load. The reason why the PCS is prone to generate excessive up-floating displacement has been found.

In the 3rd phase, the inlet speed of SCC is set as 0 m/s, and the grouting statue is shown in Figure 10. The buoyancy on PCS instantly drops to the vicinity of its gravity load. Then, a correction happens to the liquid level of SCC in the observation hole due to the residual air exits in the space of the grouting layer being filled with SCC, and the buoyancy on PCS decreases slowly. The maximum buoyancy is 16.65 kN, which is 103.3% of its gravity load.

3.3 Parameter influence analysis

To find the main factors that control the buoyancy, the parameter influence analysis is carried out. The following factors were considered, including the flowability and the inlet speed of SCC (Su *et al.*, 2024). In the end, the measures to reduce the buoyancy were proposed.

3.3.1 Flowability of SCC. The flowability of SCC can be changed by rheological parameters, including the yield shear stress τ_0, the consistency index k and the flow behavior index n.

The yield shear stress τ_0 is selected as 20, 30, 40 and 50 Pa, respectively. The maximum buoyancy is shown in Figures 11. The maximum buoyancy gradually increases as the yield

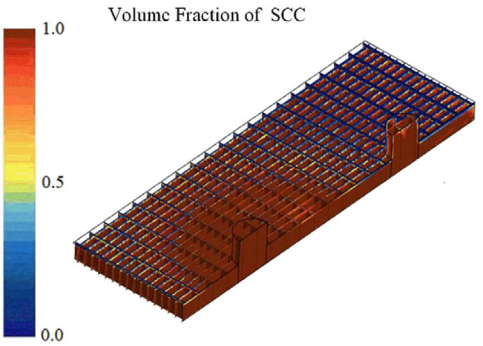

Source(s): Authors' own work

Figure 10. The grouting statue at 3rd phase

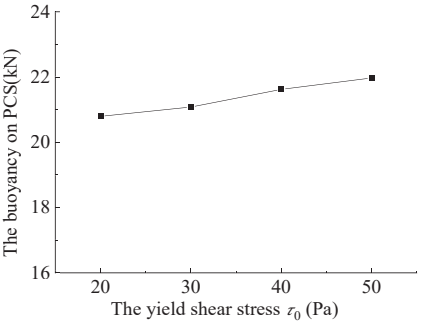

Source(s): Authors' own work

Figure 11. The buoyancy on PCS under different yield shear stress

shear stress increases. The maximum buoyancy on PCS under different yield shear stresses is 20.80, 21.08, 21.62 and 21.97 kN, respectively, which are 129.0, 130.8, 134.1 and 136.3% of its gravity load.

The consistency index k is selected as 50Pa·s$^{1.38}$, 60Pa·s$^{1.38}$, 70Pa·s$^{1.38}$, 80Pa·s$^{1.38}$ and 90Pa·s$^{1.38}$, respectively. The maximum buoyancy is shown in Figure 12. The maximum buoyancy also gradually increases as the consistency index increases. The maximum buoyancy on PCS under different consistency indexes is 20.25, 20.80, 21.08, 21.38 and 21.89 kN, respectively, which are 125.6, 129.0, 130.8, 132.6 and 135.8% of its gravity load.

The flow behavior index n is selected as 1.2, 1.3, 1.4, 1.5 and 1.6, respectively. The maximum buoyancy is shown in Figure 13. The buoyancy gradually increases as the flow behavior index increases. The maximum buoyancy on PCS under different flow behavior indexes is 20.84, 20.95, 21.08, 21.23 and 21.53 kN, respectively, which are 129.3, 130.0, 130.8, 131.7 and 133.6% of its gravity load.

In summary, the buoyancy gradually decreases as the flowability of SCC increases. Increasing the flowability of SCC is recommended to reduce the buoyancy under the condition that no segregation phenomenon happens to the aggregates of SCC in the grouting process. Meanwhile, it should be noticed that the increased flowability of SCC does not significantly reduce the buoyancy.

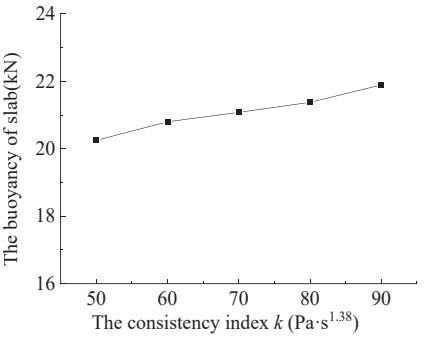

Source(s): Authors' own work

Figure 12. The buoyancy on PCS under different consistency index

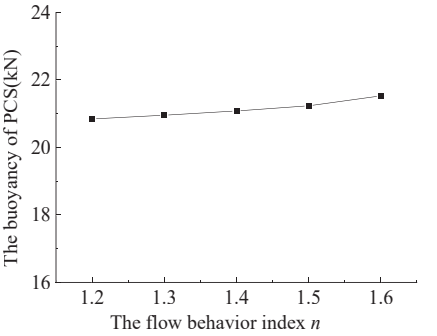

Source(s): Authors' own work

Figure 13. The buoyancy on PCS under different flow behavior index

3.3.2 Inlet speed of SCC. Different inlet speeds of SCC are considered, including 0.02, 0.04, 0.06, 0.08 and 0.1 m/s. The maximum buoyancy on PCS under different inlet speeds is shown in Figure 14.

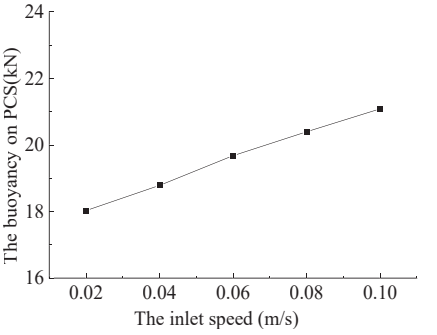

Source(s): Authors' own work

Figure 14. The buoyancy on PCS under different inlet speed of SCC

The buoyancy on PCS significantly increases as the inlet speed of SCC increases, and there is an approximate linear relationship between them. The maximum buoyancy under different inlet speeds of SCC is 18.03, 18.79, 19.68, 20.39 and 21.09 kN, respectively, which are 111.8, 116.5, 122.1, 126.5 and 130.8% of its gravity load. Considering that the maximum buoyancy appears in the later stage of the second phase, it's suggested to reduce the inlet speed of SCC during the later period of the grouting process.

The evolution characteristics of buoyancy on PCS under varying and constant inlet speed of SCC are shown in Figure 15. The initial inlet speed of SCC is 0.1 m/s, and it changes to 0.02 m/s when the liquid level of SCC is even with the bottom rim of the observation hole. The maximum buoyancy under varying and constant inlet speed of SCC is 21.09 and 18.71 kN, which are 130.8 and 111.8% of its gravity load, respectively. The buoyancy has been decreased significantly.

4. Structural optimization

Although the buoyancy on PCS has been decreased significantly by adopting varying inlet velocity of SCC, the steel beams still need to be installed in the grouting process to prevent the excessive up-floating displacement of PCS, which will lead to low construction efficiency. An optimized track structure is proposed to avoid generating larger buoyancy in the grouting process, as shown in Figure 16. No molds and steel beams are installed in the grouting process. The air can be discharged freely around the PCS.

4.1 Numerical simulation of grouting process after optimization

For an optimized track structure, the CFD model to simulate the grouting process is established, as shown in Figure 17. The evolution characteristic of buoyancy on PCS was analyzed. The size of PCS is 3,450 mm × 2,200 mm × 330 mm. The total mass is 5,667 kg. Thus, the gravity load for half of PCS is 27.77 kN.

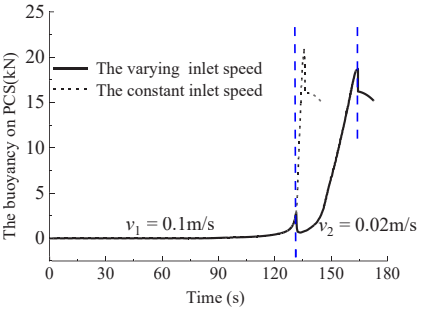

Source(s): Authors' own work

Figure 15. The buoyancy on PCS with varying and constant inlet speed of SCC

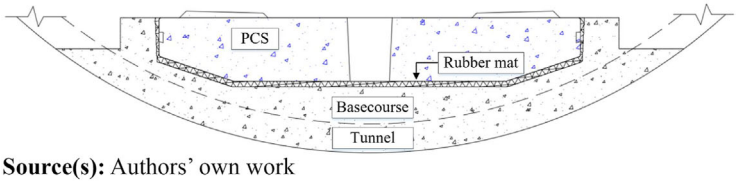

Source(s): Authors' own work

Figure 16. The optimized track structure

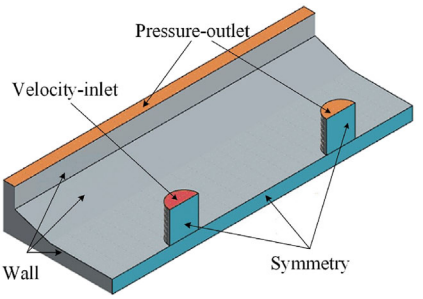

Source(s): Authors' own work

Figure 17. The CFD model to simulate the grouting process for optimized track structure

One grouting hole on PCS is set as the velocity inlet of SCC. The other one and the top surface are set as pressure outlets of air. The surface along the longitudinal centerline is set as symmetry. Other surfaces are set as a wall. The initial inlet speed of SCC is also assumed as 0.1 m/s. The evolution characteristic of buoyancy on PCS obtained from the simulation is shown in Figure 18.

It can be seen that the evolution characteristics of buoyancy are similar to the track structure before optimization. The maximum buoyancy on PCS has been decreased closely to its gravity load. The maximum buoyancy is 29.12 kN, which is 104.9% of its gravity load.

4.2 Field test results

To validate the simulation results, the field test of the grouting process is carried out for the optimized track structure. The vertical displacements of PCS were monitored in the test. The total number of PCS is 8. The total number of measuring points on one PCS is 4. The installation positions of sensors are shown in Figure 19.

The final up-floating displacement results of PCS in the grouting process are listed in Table 1. The final up-floating displacements of all PCS do not exceed 2 mm, meeting the demands of the construction criterion. In simulation, the maximum buoyancy on PCS in the grouting process is close to its gravity load. The field test and the simulation results have a good agreement.

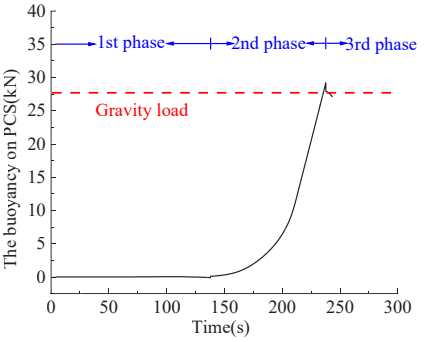

Source(s): Authors' own work

Figure 18. The time-history curve of the buoyancy on PCS

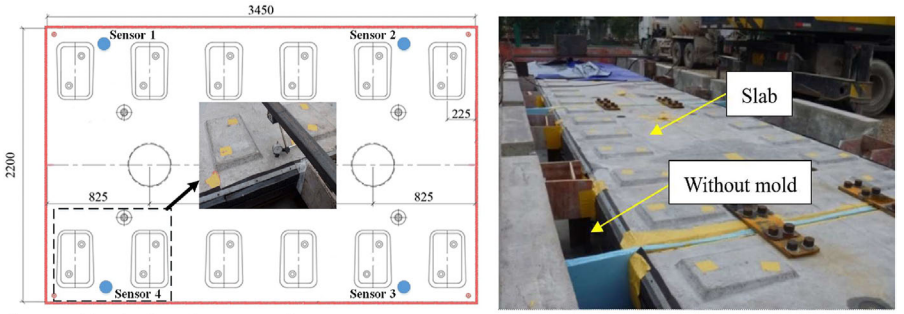

Source(s): Authors' own work

Figure 19. The installation positions of sensors on PCS

Table 1. The finial upward deformation results of PCS in field test

The number of PCS	The number of sensor	Displacement (mm)	The average (mm)
1	1	0.6	0.73
	2	0.8	
	3	1.0	
	4	0.5	
2	1	0.2	0.68
	2	1.2	
	3	0.2	
	4	1.1	
3	1	0.2	0.20
	2	0.1	
	3	0.2	
	4	0.3	
4	1	0.1	0.15
	2	0.1	
	3	0.4	
	4	0	
5	1	1.5	0.88
	2	0.4	
	3	1.2	
	4	0.4	
6	1	1.6	1.65
	2	1.6	
	3	1.8	
	4	1.6	
7	1	1.6	1.75
	2	1.9	
	3	1.6	
	4	1.9	
8	1	0.6	0.85
	2	0.1	
	3	1.1	
	4	1.6	

Source(s): Authors' own work

5. Conclusions

The grouting process of the typical PST was simulated in this paper. The evolution characteristics of buoyancy on PCS were analyzed. The key factors affecting the buoyancy were determined by parameter influence analysis. The measures to reduce the buoyancy are

proposed, and a structural optimization scheme for PST was designed to reduce the buoyancy. The characteristics of buoyancy on PCS after optimization were demonstrated both by simulation and field tests. The conclusions are drawn as following:

(1) The H-B model can accurately describe the flowability of fresh SCC. The SCC slump results of in the simulation and test have a good agreement.

(2) The evolution characteristic of buoyancy on PCS can be divided into three phases. In the first phase, no buoyancy generates. In the second phase, the buoyancy gradually increases to the maximum. In the third phase, the correction happens to buoyancy. The rapid increase in buoyancy is mainly concentrated in the later stage of the second phase.

(3) The maximum buoyancy on PCS in the simulation is 130.8% of its gravity load. It is the reason why the PCS is prone to generate the excessive up-floating displacement in the grouting process.

(4) The buoyancy reduced slightly with the increased flowability of SCC. It was mainly controlled by the inlet speed of SCC. In the later stage of the grouting process, reducing the inlet speed of SCC is recommended.

(5) For optimized track structure, the simulation results showed that the buoyancy on PCS has reduced significantly compared with its gravity load. The simulation results have a good agreement with the field test results without considering steel limiting beams and the mold.

References

Abedi, M., Lin, C., & Ji, G. (2023). Numerical simulation of casting process of fiber reinforced self-compacting concrete (SCC). In A. Ilki, D. Çavunt, & Y. S. Çavunt (Eds), *Building for the Future: Durable, Sustainable, Resilient* (Vol. 349, pp. 1601–1612). Nature Switzerland: Springer. doi: 10.1007/978-3-031-32519-9_161.

Ando, K., Sunaga, M., Aoki, H., & Haga, O. (2001). Development of slab tracks for Hokuriku Shinkansen line. *Quarterly Report of RTRI*, *42*(1), 35–41. doi: 10.2219/rtriqr.42.35.

Cao, X. (2020). Construction technology of self-compacting concrete perfusion in urban metro underground line. *Construction Technology*, *1*, 209–213.

Chen, L., Wang, Y., He, Z., Zhai, Z., & Bai, Y. (2024). Research on dynamic characteristics of railway side-cracked slab for train-track coupled system. *Engineering Failure Analysis*, *160*, 108241. doi: 10.1016/j.engfailanal.2024.108241.

Chen, W., Zhang, Y., Li, D., Pan, Z., & Lou, P. (2024). Research on crack propagation of CRTS III track slabs under train load. *Engineering Failure Analysis*, *157*, 107896. doi: 10.1016/j.engfailanal.2023.107896.

Guo, W., Huang, X., Zhao, L., & Wei, Y. (2021). Transverse cracking of concrete base plate in CRTS III ballastless track structure: Effects of environmental boundary conditions. *Applied Sciences*, *11*(21), 10400. doi: 10.3390/app112110400.

Jiang, B., Ma, M., Li, M., Liu, W., & Li, T. (2019). Experimental study of the vibration characteristics of the floating slab track in metro turnout zones. *Proceedings of the Institution of Mechanical Engineers, Part F: Journal of Rail and Rapid Transit*. (Vol. 233, pp. 1081–1096). doi: 10.1177/0954409719826824.

Jiang, W., Xie, Y., Wu, J., & Long, G. (2020). Influence of age on the detection of defects at the bonding interface in the CRTS III slab ballastless track structure via the impact-echo method. *Construction and Building Materials*, *265*, 120787. doi: 10.1016/j.conbuildmat.2020.120787.

Jiang, W., Xie, Y., Wu, J., Guo, J., & Long, G. (2021). Identifying bonding interface flaws in CRTS III type ballastless track structure using the impact-echo method. *Engineering Structures*, *227*, 111429. doi: 10.1016/j.engstruct.2020.111429.

Li, J., & Xu, W. (2013). A CFD simulation of Self-Compacting Concrete based on Herschel-Bulkley rheological model. *Gongcheng Lixue/Engineering Mechanics*, *30*(1), 373–377.

Li, H., Huang, F., Xie, Y., Yi, Z., & Wang, Z. (2017). Effect of water–powder ratio on shear thickening response of SCC. *Construction and Building Materials*, *131*, 585–591. doi: 10.1016/j.conbuildmat.2016.11.061.

Li, Y., Mu, J., Wang, Z., Liu, Y., & Du, H. (2021). Numerical simulation on slump test of fresh concrete based on lattice Boltzmann method. *Cement and Concrete Composites*, *122*, 104136. doi: 10.1016/j.cemconcomp.2021.104136.

Liang, L., Li, X., Yin, J., Wang, D., Gao, W., & Guo, Z. (2019). Vibration characteristics of damping pad floating slab on the long-span steel truss cable-stayed bridge in urban rail transit. *Engineering Structures*, *191*, 92–103. doi: 10.1016/j.engstruct.2019.04.032.

Liang, L., Li, X., Sun, Y., Gong, Z., & Bi, R. (2022). Measurement research on vibro-acoustic characteristics of large-span plate-truss composite bridge in urban rail transit. *Applied Acoustics*, *187*, 108518. doi: 10.1016/j.apacoust.2021.108518.

Mu, J., Li, Y., Hao, J., Liu, Y., & Shen, J. (2023). Research on discrete element simulation of slump test for fresh self-compacting concrete. *Journal of Building Engineering*, *70*, 106464. doi: 10.1016/j.jobe.2023.106464.

Ou, C., & Chen, Y. (2017). The control of up-floating dispalcement for CRTS II slab track during the constrcution process. *China Metal Bulletin*, *11*, 114–115.

Ren, H. (2021). Research on construction technology of metro slab track self-compacting concrete. *Railway Construction Technology*, *4*, 23–27.

Roussel, N. (2007). Correlation between yield stress and slump: Comparison between numerical simulations and concrete rheometers results. *Materials and Structures*, *39*(4), 501–509. doi: 10.1617/s11527-005-9035-2.

Su, M., Chong, Q., Xie, H., Xie, Y., & Zeng, Z. (2024). On the deformation of CRTS-III ballastless track during the casting process of self-compacting concrete: Numerical simulations and random forest-based prediction models. *Engineering Structures*, *307*, 117870. doi: 10.1016/j.engstruct.2024.117870.

Tan, Y., Xie, Y., Yang, L., & Li, L. (2017). Study and application of self-compacting concrete for HSR CRTS III slab ballastless track. *China Railway*, *8*, 21–27.

Wang, J., Gao, L., Zhao, W., Zhong, Y., Tong, F., & Wang, Q. (2022). Evolution mechanism of interlayer fatigue properties of CRTS III slab track. *Construction and Building Materials*, *360*, 129459. doi: 10.1016/j.conbuildmat.2022.129459.

Xie, H., Wei, X., Liu, X., & Liu, F. (2023). Analysis of fluid dynamic behavior and impact load on oblique water entry of a two-dimensional seaplane based on VOF method. *Ocean Engineering*, *274*, 114028. doi: 10.1016/j.oceaneng.2023.114028.

Xu, G., Liu, X., Yang, R., & Yang, J. (2013). Reasons for displacement of ballastless track slab during self-compacting concrete pouring. *Journal of Southwest Jiaotong University*, *48*(1), 42–46.

Zhang, K., Yuan, Q., Huang, T., Zuo, S., Chen, R., & Wang, M. (2022). Predicting the cracking behavior of early-age concrete in CRTS III track. *Construction and Building Materials*, *353*, 129105. doi: 10.1016/j.conbuildmat.2022.129105.

Zhang, Y., Zhang, H., Wu, K., Cai, X., Guo, Q., Gao, L., & Jiang, J. (2024). Mechanical characteristics of track slab and clamps during the pouring of self-compacting concrete in the China Railway Track System III slab track. *Structures*, *67*, 106996. doi: 10.1016/j.istruc.2024.106996.

Corresponding author
Tao Xin can be contacted at: xint@bjtu.edu.cn

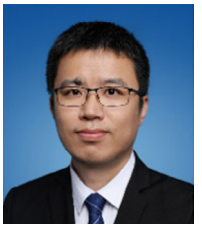

Tao Xin was awarded his Ph.D degree from Beijing Jiaotong University, where he currently serves as a professor. His scholarly work centers on addressing critical challenges in railway track dynamics, continuous welded rail and vibration reduction track. He won the first-class prize of National Scientific and Technological Progress Award in 2017.